Oxygen pressure modulated magnetism and magnetic anisotropy of epitaxial transparent Yb$_2$Ti$_2$O$_7$ pyrochlore films

Ming-Yuan Yan,[1] Zhen-Tao Pang [⑩],[1] Zhao-Cai Wang [⑩],[2] Zhong-Nan Xi,[1] Li- Da Chen,[1] Xiao-Yu Zhang,[1] Yu-Qi Wang,[1] Ren-Kui Zheng,[3] Yu Deng,[1,*] and Shan-Tao Zhang [⑩][1,†]

[1]*National Laboratory of Solid State Microstructures, College of Engineering and Applied Science & Jiangsu Key Laboratory of Artificial Functional Materials & Collaborative Innovation Center of Advanced Microstructures, Nanjing University, Nanjing 210093, China*
[2]*School of Materials Science and Engineering and Jiangxi Engineering Laboratory for Advanced Functional Thin Films, Nanchang University, Nanchang 330031, China*
[3]*School of Physics and Materials Science, Guangzhou University, Guangzhou 510006, China*

Pyrochlore Yb$_2$Ti$_2$O$_7$ has gained significant attention due to the low-temperature geometrical frustration induced unusual magnetic phase. Most experimental studies on Yb$_2$Ti$_2$O$_7$ have been performed on polycrystalline bulk or single crystals; however, there have been a few reports detailing the structure and magnetism of Yb$_2$Ti$_2$O$_7$ thin films. Here, we fabricated high-quality (001)-, (110)-, and (111)-epitaxial transparent Yb$_2$Ti$_2$O$_7$ films on single-crystal yttria-stabilized ZrO$_2$ (YSZ) substrates with various oxygen pressures by pulsed laser deposition. Structural characterizations confirm flat surface and uniform and well-defined atomic arrangement of the Yb$_2$Ti$_2$O$_7$ films, as well as atomic-scale epitaxial and sharp Yb$_2$Ti$_2$O$_7$/YSZ interface. The (111) oriented films fabricated at 10 Pa oxygen pressure have the highest magnetization value of 2.03 μ_B/Yb, which is higher than that of bulk counterparts, due to the fact that the distorted Yb-tetrahedra induced by interfacial strain and defects can destroy magnetic frustration and enhance magnetization. Especially, the fabricated (001)-, (110)-, and (111)-epitaxial Yb$_2$Ti$_2$O$_7$ films illustrate a significantly pronounced magnetic anisotropy, which results from the single ion anisotropy of Yb and the anisotropic exchange interactions. In addition, a wide-spectrum transmittance of ~95% was achieved in (110)-epitaxial Yb$_2$Ti$_2$O$_7$ films, which is comparable to the state-of-the-art transparent materials. Our work gives a comprehensive perspective on the structure, magnetism, magnetic anisotropy, and transmittance of Yb$_2$Ti$_2$O$_7$ films, which may guide further work on pyrochlore materials.

I. INTRODUCTION

Magnetism affected by geometrical frustration has received considerable attention due to the induced unusual and new magnetic phases [1,2]. The rare-earth titanate pyrochlores R_2Ti$_2$O$_7$, where R is a trivalent rare-earth element (R = La, Ce, Pr, …, Lu), form a family in which a wide variety of exciting physical phenomena can be explored [3,4]. Specifically, taking Yb$_2$Ti$_2$O$_7$ as an example, the rare-earth Yb ions form a magnetic network of corner-sharing tetrahedra and lead to a highly frustrated pyrochlore lattice, as shown in Fig. 1(a). Furthermore, depending on the balance among the subtle interplay of energy terms such as those of the rare-earth ions, the anisotropy of the spins, as well as the exchange and dipolar interactions, complex magnetic orders such as first order transition (R = Gd, Er), spin liquid (R = Tb), and spin ice (R = Ho, Dy) have been observed [5,6].

Besides the corner-sharing tetrahedra, the oxygen environment around different cations also plays an important role in Yb$_2$Ti$_2$O$_7$ properties. As shown in Fig. 1(b), six oxygen ions occupy the 48f-Wycoff sites around the Yb ion, commonly referred to as O(1), and are displaced in two antiparallel planar triangles with a threefold rotation axis [7]. Two oxygen ions occupy the 8b-Wycoff sites, referred to as O(2), and are located at the center of the tetrahedron formed by the Yb ion. The eight oxygen ions surround the Yb ion and form a distorted cube along the local [111] axis. In contrast, the oxygen environment of the Ti ion consists of a trigonal antiprism of six O(1) oxygen ions. Indeed, particular occupancies of the oxygen ions in the pyrochlore structure can be partially absent [8,9], which may not lead to the collapse of the pyrochlore structure, but tends to result in a different crystal field environment around the Yb ions, leading to magnetic anisotropy of the rare-earth titanate pyrochlores.

As a member of the rare-earth titanate pyrochlore family, Yb$_2$Ti$_2$O$_7$ has been proposed to be a good candidate for a quantum version of spin ice [10]. Much effort has focused on the magnetic ground states and related magnetic properties of Yb$_2$Ti$_2$O$_7$, which is, however, still controversial at present [11–13]. For example, there is reported evidence for either a dynamically disordered ground state or an ordered low-temperature ferromagnetic state [12,14]. Another interesting feature of Yb$_2$Ti$_2$O$_7$ is that the magnetic properties are very sensitive to defects. This has been demonstrated in some non-stoichiometric Yb$_2$Ti$_2$O$_7$ pyrochlores, such as Yb$_2$Ti$_2$O$_{7-\delta}$, Yb$_2$(Ti$_{2-x}$Yb$_x$)O$_{7-x/2}$, and Yb$_{2+x}$Ti$_{2-x}$O$_{7-\delta}$ [15,16]. In addi-

*Corresponding author: dengyu@nju.edu.cn
†Corresponding author: stzhang@nju.edu.cn
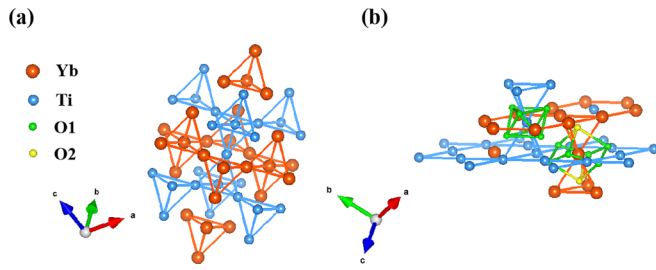
FIG. 1. (a) Schematic diagram of the corner-sharing tetrahedral network in $Yb_2Ti_2O_7$. (b) Comparison of the A-site and B-site oxygen environments in $Yb_2Ti_2O_7$.

tion, the application of chemical stress can effectively perturb the quantum spin fluctuations of the Yb ions and lead to different magnetic ground states [17]. Recently, the introduction of isolated oxygen vacancy has been reported to stabilize the spin-liquid phase, and annealing samples in oxygen is a method to suppress oxygen vacancy to obtain ultrapure samples [16]. To further clarify the effects of oxygen pressure, a promising way is to systematically investigate the structure and properties of $Yb_2Ti_2O_7$ prepared under different oxygen pressures.

On the other hand, some studies have predicted the presence of large magnetic anisotropy in $Yb_2Ti_2O_7$ [10,18–20]. For example, the effective anisotropic spin-1/2 Hamiltonian has been determined by modeling the high-field neutron spin-wave dispersion intensities [10]. The molecular field tensor of $Yb_2Ti_2O_7$ has been shown to be strongly anisotropic by polarized neutron diffraction at very low temperatures [18]. A set of crystal field parameters and anisotropic exchange coupling constants have been investigated in the framework of crystal field theory and mean field approximation [19]. These studies indirectly illustrate the magnetic anisotropy by theoretical calculations or analyses based on bulk $Yb_2Ti_2O_7$, but lack direct experimental evidence of the magnetic anisotropy. Therefore, a systematically experimental study on the magnetic anisotropy of $Yb_2Ti_2O_7$ is highly desirable.

Epitaxial thin film provides a suitable platform for the study of not only oxygen vacancy related structure and magnetism but also magnetic anisotropy, as the crystallographic orientation and oxygen vacancy concentration of $Yb_2Ti_2O_7$ films can be easily controlled by epitaxial growth on substrates with different orientations under different oxygen pressures. Recently, the pyrochlore thin films of $Pr_2Ir_2O_7$, $Y_2Ir_2O_7$, and $Y_{1.7}Bi_{0.3}Ir_2O_7$ were fabricated on cubic (001)-, (011)-, and (111)-oriented yttria-stabilized ZrO_2 (YSZ) single crystal substrates with lattice parameters $a = b = c \sim$ 5.125 Å [21,22]. It is noted that $Yb_2Ti_2O_7$ has a similar cubic crystal structure ($a = b = c = 10.03$ Å in bulk single crystal) [9], which makes it very possible to be epitaxially grown on YSZ single crystal substrates. Moreover, the interface strain due to film/substrate lattice mismatch and oxygen vacancy can be induced as extra freedom degrees to tune properties.

In this paper, we have fabricated (001)-, (110)-, and (111)-epitaxial $Yb_2Ti_2O_7$ films on YSZ single-crystal substrates by pulsed laser deposition (PLD) with different oxygen pressures from 2×10^{-4} to 10 Pa. Structure characterizations prove the high crystallinity and uniformity of $Yb_2Ti_2O_7$ films and

sharpness of the interfaces. The (111) oriented films fabricated at 10 Pa show the highest magnetization of $2.03\mu_B/Yb$, which is affected by lattice distortion and defects. Moreover, a strong magnetic anisotropy is demonstrated in the (001)-, (110)-, and (111)-epitaxial $Yb_2Ti_2O_7$ films, which arises from the single ion anisotropy of Yb and the anisotropic exchange interactions. In addition, wide-spectrum (325–2500 nm) optical transmission of ∼95% was observed in the (110)-oriented $Yb_2Ti_2O_7$ films.

II. RESULTS AND DISCUSSION

The x-ray diffraction (XRD) θ-2θ scan patterns of the $Yb_2Ti_2O_7$/YSZ(111) heterostructures fabricated at different substrate temperatures under a fixed oxygen pressure of 2×10^{-4} Pa are plotted in Fig. S(2) within the Supplemental Material [23]. One can see that all detectable diffraction peaks are attributed to substrates and thin films, implying that the thin films are single phase. Especially, with increasing temperature, the diffraction peaks arising from thin films not only shift toward high angle, but also become sharp and intense. Further rocking curves taken on the (222) diffraction peak of the thin films fabricated at 600 and 650 °C, as illustrated in the insets of Fig. S(2) within the Supplemental Material [23], show low full width at half maximum (FWHM) values of 0.0632° and 0.0627°, respectively. This observation implies that the optimal substrate temperature for fabricating high quality $Yb_2Ti_2O_7$ thin films is ∼650 °C.

Figure 2(a) shows the XRD θ-2θ scan patterns of the $Yb_2Ti_2O_7$/YSZ(111) heterostructures fabricated at fixed temperature of 650 °C but different oxygen pressures ($P_g = 10$, 1, 0.1, and 2×10^{-4} Pa). Only YSZ (111), (222), and $Yb_2Ti_2O_7$ (111), (222), (444) diffraction peaks are detected, implying that the $Yb_2Ti_2O_7$ films are single phase and highly (*lll*) oriented. The presence of a (111) diffraction peak affirms the excellent crystallization of the pyrochlore phase, as the pyrochlore phase is the superstructure of the fluorite structure, which has been demonstrated in previous literatures on pyrochlores [24]. One can see from Fig. 2(a) that the intensity of (111) diffraction peak of $Yb_2Ti_2O_7$ films significantly decreases as the oxygen pressure increases, suggesting that the film grown under 10^{-4} Pa has the least cation disorder.

Figure 2(b) plots the locally magnified XRD pattern around $2\theta \sim 30°$, which shows distinct Laue oscillations near the $Yb_2Ti_2O_7$ (222) diffraction peaks. The presence of Laue oscillations is taken as evidence that grown films are of high quality and are homogenous [25,26]. Moreover, the x-ray reflectivity (XRR) of the films fabricated at 10 and 2×10^{-4} Pa oxygen pressure exhibits obvious Kiessig fringes at low diffraction angles, as shown in Fig. 2(c). The Kiessig fringes become unresolvable at $2\theta \sim 5°$, indicating a small interface roughness [27,28]. This is in good agreement with the root-mean-square roughness around 89–131 pm of these four $Yb_2Ti_2O_7$ films revealed by atomic force microscopy (AFM) images Fig. S(3) within the Supplemental Material [23]). The full width at half maximum (FWHM) of XRD rocking curves taken on the $Yb_2Ti_2O_7$ (222) diffraction peaks are close to 0.06° [Fig. 2(d) and the inset]. All these characterizations prove that the fabricated $Yb_2Ti_2O_7$ thin films have a high degree of crystallinity.

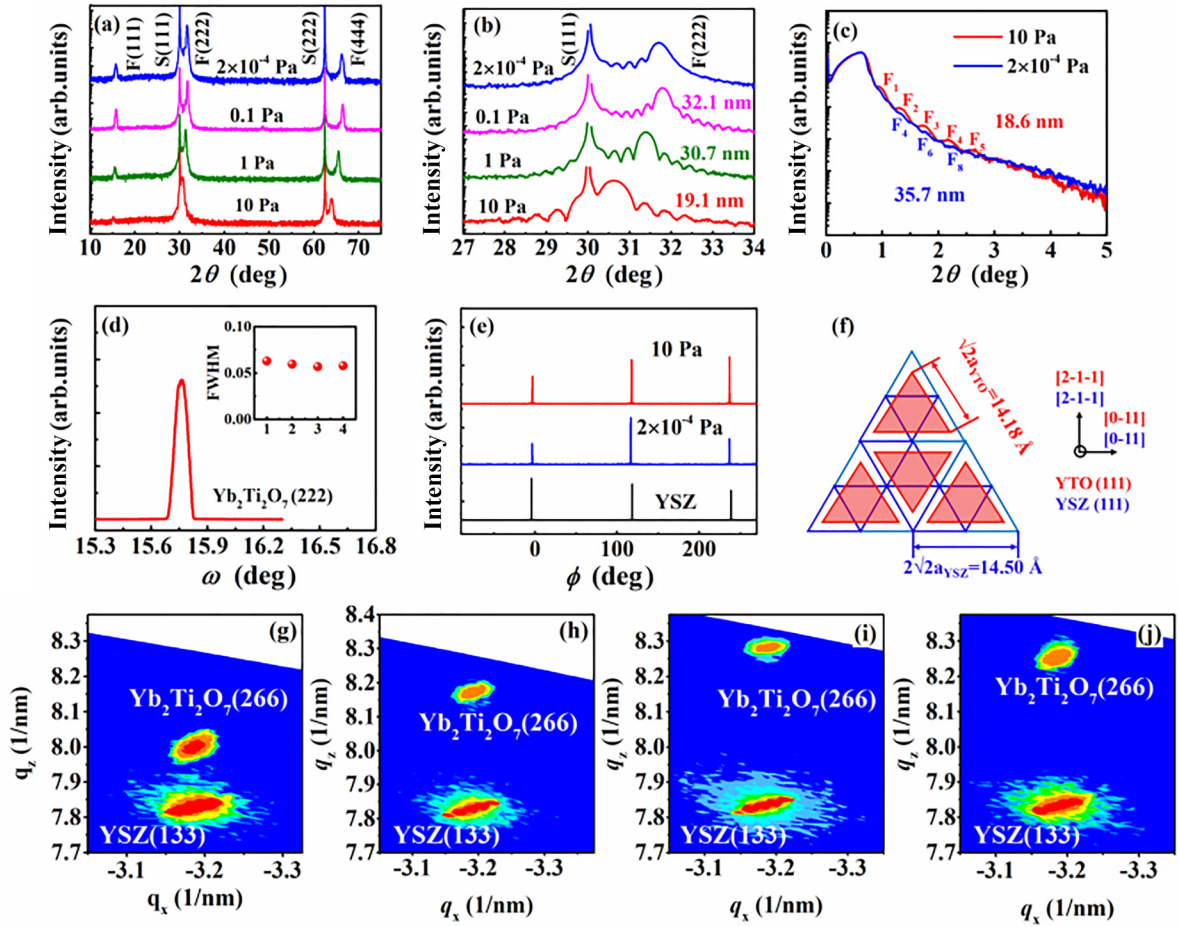FIG. 2. (a) XRD θ-2θ scan patterns of $Yb_2Ti_2O_7$ films fabricated on YSZ (111) at 650 °C but at different oxygen pressures P_g. Here, F and S represent the $Yb_2Ti_2O_7$ film and YSZ substrate, respectively. (b) High-resolution XRD scans of the films near the (222) peak. (c) High-resolutiuon XRR of $Yb_2Ti_2O_7$ films fabricated at $P_g = 10$ and 2×10^{-4} Pa. (d) XRD rocking curves taken on the $Yb_2Ti_2O_7$ (222) diffraction peaks. The inset shows the FWHM values, where 1, 2, 3, and 4 represent the $Yb_2Ti_2O_7$ films fabricated at $P_g = 10$, 1, 0.1, and 2×10^{-4} Pa, respectively. (e) XRD φ scan patterns of $Yb_2Ti_2O_7$/YSZ(111) heterostructure fabricated at $P_g = 10$ and 2×10^{-4} Pa. (f) Schematic illustration of in-plane lattice arrangements of $Yb_2Ti_2O_7$ unit cells on a YSZ(111) substrate. (g)–(j) RSMs of the (111)-epitaxial $Yb_2Ti_2O_7$ film fabricated at $P_g = 10$, 1, 0.1, and 2×10^{-4} Pa.

Furthermore, as examples, the in-plane crystallographic orientations of the $Yb_2Ti_2O_7$ films ($P_g = 10$ and 2×10^{-4} Pa) with respect to the YSZ(111) substrate around the (440) diffractions are examined by XRD φ scans. In Fig. 2(e), threefold symmetrical diffraction peaks are observed for the $Yb_2Ti_2O_7$ film and the YSZ(111) substrate, which shows that the $Yb_2Ti_2O_7$ films are epitaxially grown on the YSZ(111) substrates. The reciprocal space mappings (RSMs) around the (133) peak of substrates, together with the $Yb_2Ti_2O_7$ films fabricated at 10, 1, 0.1 and 2×10^{-4} Pa oxygen pressure, are plotted in Figs. 2(g)–2(j), respectively. It can be seen that the (266) diffraction of the film shares the same in-plane lattice parameters with the YSZ substrate for all films, indicating that the epitaxial $Yb_2Ti_2O_7$ film has been coherently strained on the YSZ substrate. In addition, with decreasing oxygen pressure, the position of (266) diffraction varies in the vertical direction in RSMs; namely, the q_z value significantly increases from 8.02 to 8.291/Å, suggesting the decrease of out-of-plane lattice of $Yb_2Ti_2O_7$ films. This is also clearly reflected by the fact that the diffraction

peaks move towards higher angles as P_g decreases from 10 to 2×10^{-4} Pa. As schematically illustrated in Fig. 2(f), the in-plane epitaxial relationships between film and substrate are determined to be $[0-11]Yb_2Ti_2O_7 // [0-11]$YSZ and $[2-1-1]Yb_2Ti_2O_7 // [2-1-1]$YSZ, respectively.

In addition to the general structural information from Laue oscillations and Kiessig fringes, these two oscillations in Figs. 2(b) and 2(c) can also be used to calculate the film thickness using the following Eqs. (1) and (2), respectively [29]:

$$t = \frac{[(n+1) - n]\lambda}{2(\sin\theta_{n+1} - \sin\theta_n)}, \tag{1}$$

$$\frac{(2n+1)\lambda^2}{4t^2} = \theta_{n+1}^2 - \theta_n^2, \tag{2}$$

where t is the film thickness, n and $n+1$ are the orders of two neighboring oscillations, and λ is 1.5406 Å. The calculated thicknesses of the $Yb_2Ti_2O_7$ films fabricated at 10, 1, 0.1, and 2×10^{-4} Pa oxygen pressure are 19, 31, 32, and 36 nm, respectively. Please note that for each film the thicknesses
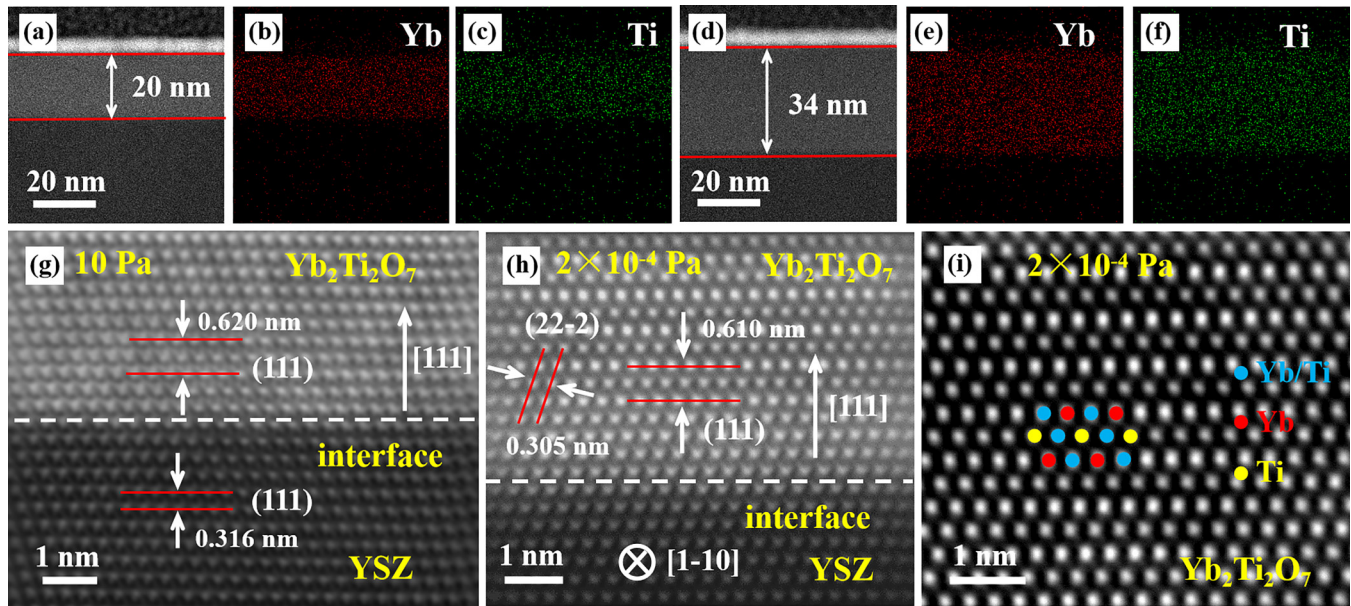
FIG. 3. (a) and (d) Low-magnification HAADF-STEM images of the interface of $Yb_2Ti_2O_7$/YSZ(111) heterostructures fabricated at $P_g = 10$ and 2.0×10^{-4} Pa. The elemental mapping of [(b),(e)] Yb and [(c),(f)] Ti elements for the corresponding $Yb_2Ti_2O_7$ film fabricated at $P_g = 10$ and 2.0×10^{-4} Pa obtained by STEM-enenrgy dispersive spectroscopy (EDS). (g)–(h) Cross-sectional HAADF-STEM images of the $Yb_2Ti_2O_7$/YSZ(111) heterostructure fabricated at $P_g = 10$ and 2.0×10^{-4} Pa. (i) Enlarged HAADF-STEM image of the $Yb_2Ti_2O_7$ film fabricated at $P_g = 2.0 \times 10^{-4}$ Pa. The Yb and Ti atomic positions labeled in the selected areas are consistent with pyrochlore structure. The blue dots represent the mixed Yb and Ti column due to the alternating arrangement along zone axis.

calculated from the two equations are close, for example those of the films fabricated at $P_g = 10$ Pa are 19.1 and 18.6 nm calculated from the two equations, respectively.

To avoid possible error, the thickness of (111)-epitaxial $Yb_2Ti_2O_7$ films is also measured by transmission electron microscopy (TEM) to verify the effectiveness of XRR analysis. The cross-sectional microscopic morphologies of $Yb_2Ti_2O_7$/YSZ(111) fabricated at $P_g = 10$ and 2×10^{-4} Pa are further investigated by scanning transmission electron microscopy (STEM). Low-magnification cross-sectional high-angle annular dark-field (HAADF) STEM images [Figs. 3(a) and 3(d)] show thicknesses of ∼20 and 34 nm, respectively. The thickness values are consistent with the calculated results from XRD and XRR. The $Yb_2Ti_2O_7$ film fabricated at 10 Pa shows a thinner thickness, which may be explained by the higher oxygen pressure resulting in a higher collision rate between the oxygen atom and deposited atoms or ions [30]. Moreover, the corresponding elemental mappings of the $Yb_2Ti_2O_7$ films fabricated at $P_g = 10$ and 2×10^{-4} Pa, as shown in Figs. 3(b) and 3(e) and Figs. 3(c) and 3(f), suggest both Yb and Ti elements are uniformly distributed without any obvious secondary phase.

To further analyze the crystal structure of the $Yb_2Ti_2O_7$/YSZ heterostructures, atomic-scale HAADF images of the $Yb_2Ti_2O_7$ films fabricated at $P_g = 10$ and 2×10^{-4} Pa are obtained. As shown in Figs. 3(g) and 3(h), the $Yb_2Ti_2O_7$ film grows layer by layer along the [111] direction and shows a well-defined atomic arrangement. For clarity, the enlarged HAADF-STEM image of the $Yb_2Ti_2O_7$ film fabricated at $P_g = 2 \times 10^{-4}$ Pa is shown in Fig. 3(i), from which we can see three types of columns of atoms: one

column contains only Yb ions (red), one column contains only Ti ions (yellow), and in the another column Yb and Ti ions are alternatingly arranged (blue) along the zone axis, in good agreement with the reported structure of other pyrochlores [31]. In addition, an atomic-scale smooth and sharp $Yb_2Ti_2O_7$/YSZ interface is observed under high magnification, which agrees well with the analysis derived from the pronounced Laue oscillations and Kiessig fringes in Figs. 2(b) and 2(c). Moreover, the lattice parameters along the [111] direction of the $Yb_2Ti_2O_7$ films are measured. It can be seen from Figs. 3(g) and 3(h) that the lattice spacing of 0.620 nm corresponds to the (222) planes of the $Yb_2Ti_2O_7$ films fabricated at $P_g = 10$ Pa, which is larger than the ∼0.610 nm spacing of the films fabricated at $P_g = 2 \times 10^{-4}$ Pa, consistent with above analysis.

Figure 4(a) displays the magnetic field dependence of out-of-plane magnetization curves (M-H) of the $Yb_2Ti_2O_7$ films fabricated at $P_g = 10$ Pa, and those for $P_g = 1$, 0.1, 2×10^{-4} Pa are shown in Fig. S(4) within the Supplemental Material [23]. The magnetization response shows nearly no hysteresis between the increasing and decreasing magnetic field. The M-H curve for each film measured at 2 K has a tendency to saturate as the magnetic field increases to $H = 3$ T, exhibiting typical weak ferromagnetic behaviors [32,33]. However, the saturation trend diminishes with increasing temperature and the M-H curve appears to be almost linear at 10 K.

For comparison, Fig. 4(b) illustrates the P_g dependent out-of-plane M-H curves of $Yb_2Ti_2O_7$ films measured at 2 K. It can be seen that the maximum magnetization (M) decreases with decreasing oxygen pressure. The relative
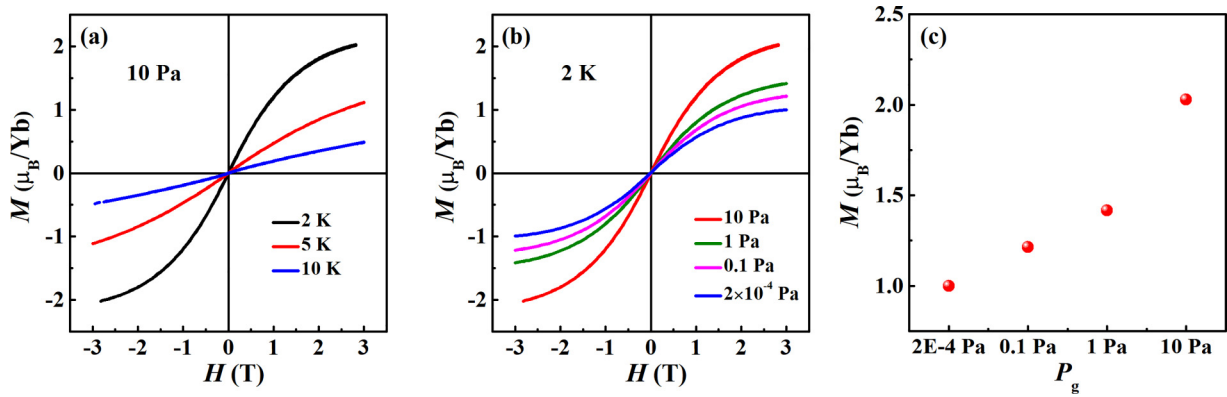
FIG. 4. (a) Out-of-plane M-H curves measured at different temperatures of the (111)-epitaxial $Yb_2Ti_2O_7$ film fabricated at $P_g = 10$ Pa. (b) The oxygen pressure-dependent out-of-plane M-H curves of (111)-epitaxial $Yb_2Ti_2O_7$ films measured at 2 K. (c) The corresponding maximum magnetization as a function of oxygen pressure (P_g) for the (111)-epitaxial $Yb_2Ti_2O_7$ films. The magnetic contribution of the YSZ substrate has been deducted from all M-H curves.

change of maximum magnetization at 3 T, $\Delta M/M$, is approximately 51% for the (111)-epitaxial $Yb_2Ti_2O_7$ films, where $\Delta M/M = [M(P_g = 10 \, \text{Pa}) - M(P_g = 2 \times 10^{-4} \text{Pa})]/M(P_g = 10 \, \text{Pa})$. A similar phenomenon was reported in $Dy_2Ti_2O_7$ single crystals in which the crystal prepared in high-vacuum environment shows a smaller magnetization [34]. In general, the change in magnetization is usually attributed to two factors: dilution effect and exchange interaction [35]. The dilution effect is not responsible for the variation in magnetization since no element substitution, and accordingly, the significant modulation of M in our case shall be due to altered exchange interaction between magnetic ions.

In order to further analyze the magnetization of films fabricated with different oxygen pressures, magnetization of (111)-epitaxial $Yb_2Ti_2O_7$ films is shown as a function of oxygen pressure in Fig. 4(c). One can see that the maximum magnetization with the value of $2.03\mu_B$/Yb occurs in the $Yb_2Ti_2O_7$ film fabricated at 10 Pa, while the magnetization value decreases with decreasing oxygen pressure. Notably, the highest magnetization value is higher than that of bulk single crystals or polycrystalline ceramics. For the $Yb_2Ti_2O_7$ films fabricated at 10 Pa, the lower intensity of the (111) diffraction peak in Fig. 1(a) indicates higher degree of cation disordering. Combined with the film/substrate interface strain, these factors would lead to distorted Yb-tetrahedra reflected by the change of out-of-plane lattice spacing. This makes the delicate magnetic interactions deviate from the magnetic spin balance of the four Yb^{3+} ions on a perfect lattice, thus it breaks the balanced frustration and results in enhanced magnetization.

To investigate orientation-dependence of the magnetic property, the (001)- and (110)-epitaxial $Yb_2Ti_2O_7$ films are fabricated at the oxygen pressures of 10 and 2×10^{-4} Pa and temperature of 650 °C. Figures 5(a) and 5(b) show the XRD θ-2θ scans of the $Yb_2Ti_2O_7$ films grown on YSZ (001) and YSZ(110) substrates at 10 Pa. Besides the diffraction peaks of YSZ substrates, only diffraction peaks stemming from the coincident orientations of $Yb_2Ti_2O_7$ films can be observed, indicating all these $Yb_2Ti_2O_7$ films are single phase and highly oriented. The sharp XRD rocking curves [insets of Figs. 5(a) and 5(b)] and flat surface revealed by AFM images (Fig. 5(g) and Fig. S(5) within the Supplemental

Material [23]) imply good crystallinity of the (001)- and (110)-oriented $Yb_2Ti_2O_7$ films. Further, the XRD φ scans and RSMs (Figs. 5(c), 5(d), 5(f), and Fig. S(6) within the Supplemental Material [23]) indicate that both the (001)- and (110)-oriented $Yb_2Ti_2O_7$ films have been epitaxially grown on the YSZ substrates. The in-plane orientation relationships of the $Yb_2Ti_2O_7$ films on (001)- and (110)-oriented YSZ substrates are determined to be [100]$Yb_2Ti_2O_7$//[100]YSZ and [010]$Yb_2Ti_2O_7$//[010]YSZ, [001]$Yb_2Ti_2O_7$//[001]YSZ and [−110]$Yb_2Ti_2O_7$//[−110]YSZ, respectively, as schematically illustrated in Fig. 5(e). Similar structural information of $Yb_2Ti_2O_7$ films fabricated at 2×10^{-4} Pa is shown in Fig. S(7) within the Supplemental Material [23].

Figure 6(a) illustrates the crystallographic orientation dependent out-of-plane M-H curves for the $Yb_2Ti_2O_7$ films fabricated at 10 and 2×10^{-4} Pa measured at 2 K. It can be seen from Fig. 6(a) that the maximum magnetization (M) of (110)-epitaxial $Yb_2Ti_2O_7$ films grown under 10 Pa is $\sim 2.91\mu_B$/Yb, larger than those of (001)- and (111)-epitaxial $Yb_2Ti_2O_7$ films, which are $\sim 1.87\mu_B$/Yb and $\sim 2.03\mu_B$/Yb respectively. This result demonstrates a clear orientation dependent magnetization, i.e., magnetic anisotropy, similar to the reported result in $Yb_2Ti_2O_7$ single crystals [36,37]. A similar magnetic anisotropy is also observed in the $Yb_2Ti_2O_7$ films fabricated at 2×10^{-4} Pa. To further investigate the magnetic anisotropy, the measuring magnetic field was applied in plane and out of plane for one sample, and the results of the (110)-epitaxial $Yb_2Ti_2O_7$ films fabricated at 10 and 2×10^{-4} Pa are comparatively plotted in Fig. 6(b), which also indicates an in-plane and out-of-plane anisotropy. For the (110)-epitaxial $Yb_2Ti_2O_7$ films, the maximum magnetization along the out-of-plane direction is much higher than that along the in-plane direction, which further indicates the magnetic anisotropy of $Yb_2Ti_2O_7$ films.

There are several microscopic mechanisms for anisotropic magnetism exemplified by magnetic dipole interaction, anisotropic exchange interactions, and single ion anisotropy [37]. However, magnetic dipole interaction is only applicable to noncubic crystals. Therefore, the observed magnetic anisotropy in this work has two possible contributions. One is the anisotropic magnetic interionic exchange. This contribu-
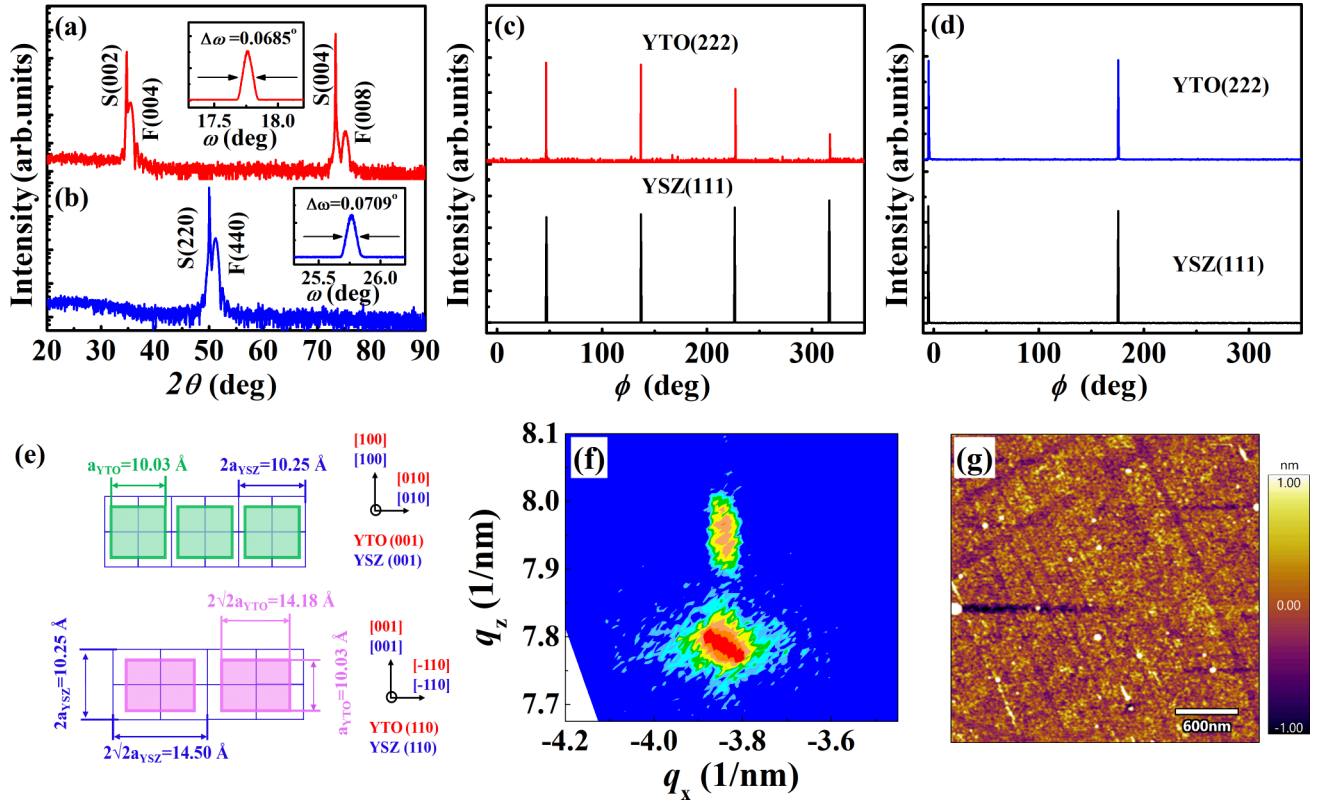
FIG. 5. (a) and (b) XRD θ-2θ scan patterns of Yb$_2$Ti$_2$O$_7$ films fabricated on (001)- and (110)-YSZ substrates at 10 Pa, respectively. Inset: XRD rocking curves are taken on the Yb$_2$Ti$_2$O$_7$ (400) and (440) diffraction peaks. (c) and (d) XRD φ scan patterns for the Yb$_2$Ti$_2$O$_7$/YSZ(001) and Yb$_2$Ti$_2$O$_7$/YSZ(110) heterostructures, respectively. (e) Illustration of in-plane lattice arrangements for Yb$_2$Ti$_2$O$_7$ unit cells on the YSZ(001) and YSZ(110) lattice plane. (f) RSM around YSZ (204) of (001)-oriented YSZ substrates. (g) The AFM image of the (001)-oriented Yb$_2$Ti$_2$O$_7$ film.

tion is similar to that in previous studies where the exchange interaction is anisotropic in small moment systems like Yb, and the dipole-dipole interactions play a minor role when considering the total inter-ionic magnetic coupling composed of the exchange and the dipole-dipole interactions between the rare earth ions [33]. The other contribution arises from the crystal field induced single ion anisotropy. For confirmation, the magnetization curve of Yb$_2$Ti$_2$O$_7$ was calculated by the Brillouin function. The inset of Fig. 6(a) comparatively presents the experimentally measured *M-H* curves

for the Yb$_2$Ti$_2$O$_7$ film fabricated at 10 Pa and theoretically calculated magnetization curves for Yb$_2$Ti$_2$O$_7$ from the Brillouin formula [38], expressed as the following equation:

$$\mu = Ng\mu_B J B_J(x), \tag{3}$$

where

$$B_J(x) = \frac{2J+1}{2J}\coth\left(\frac{2J+1}{2J}x\right) - \frac{1}{2J}\coth\left(\frac{x}{2J}\right) \tag{4}$$

μ is the magnetic moment, N is the number of magnetic atoms in the sample, $g = 8/7$ is the Lande factor of the $^2F_{7/2}$ multiplet, μ_B is the Bohr magneton, and $J = 7/2$ is the total angular momentum quantum number. $x = \frac{g\mu_B}{k_B}\frac{JH}{T}$, where H is the external magnetic field, k_B is the Boltzmann constant, and T is temperature. The experimental magnetizations of (111)-, (110)- and (100)-epitaxial films are smaller than the calculated one, which proves the single ion anisotropy effect [32]. As discussed above, the Yb ions are located in trigonally (D_{3d}) distorted scalenohedra with two kinds of oxygen, as described in Fig. 1(b). The central Yb ion is, therefore, influenced by a D_{3d} crystal electric field, which makes the energy levels of Yb ions anisotropic and leads to the magnetic property being anisotropic along different directions, thereby producing a single-ion crystal electric field magnetic anisotropy [39,40].

Due to the high quality of the Yb$_2$Ti$_2$O$_7$ films and by noting the relatively wide bandgap of Yb$_2$Ti$_2$O$_7$ [41], it is reasonable to expect Yb$_2$Ti$_2$O$_7$ films to show wide spectrum high

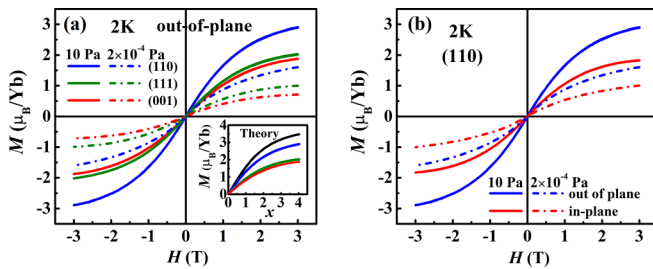
FIG. 6. (a) Out-of-plane *M-H* curves of (001)-, (110)-, and (111)-epitaxial Yb$_2$Ti$_2$O$_7$ thin films fabricated at 10 and 2×10^{-4} Pa measured at 2K. The magnetic field was applied along the out-of-plane direction (*H* perpendicular to the film surface). (b) Out-of-plane and in-plane *M-H* curves of (110)-epitaxial Yb$_2$Ti$_2$O$_7$ film measured at 2 K.
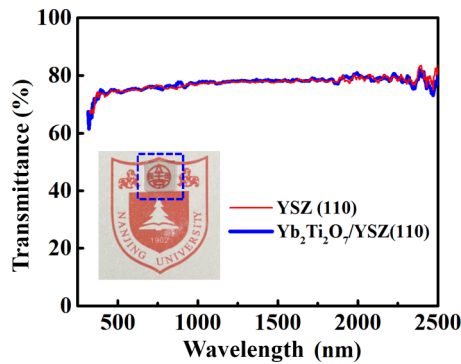
FIG. 7. The optical transmittance in the wavelength range of 325–2500 nm for the (110)-epitaxial $Yb_2Ti_2O_7/YSZ(110)$ thin-film sample fabricated at 10 Pa and a bare double-polished YSZ(110) substrate.

optical transmittance. The inserted image in Fig. 7 shows a photograph of the transparent 34 nm $Yb_2Ti_2O_7$ film fabricated on double-polished YSZ (110) substrate. It can be clearly seen that the $Yb_2Ti_2O_7$ film has a good optical transmittance within the visible region. Figure 7 shows the optical transmittance of the $Yb_2Ti_2O_7$ film in the wavelength range of 325–2500 nm. The absorption edge is at about 370 nm. The average transmittance achieves ∼75% for both $Yb_2Ti_2O_7$ film and YSZ substrate. By deducting the substrate contribution, the absolute average transmittance of $Yb_2Ti_2O_7$ films exceeds 95% in the visible region and the near-infrared range. Notably, such transmittance is significantly better than that of reported single-phase pyrochlore ceramics, such as 73.0% for $Y_2Ti_2O_7$ at 800 nm, 70.7% for $LaGdHf_2O_7$ at 1100 nm, and 74.0% for $La_2Hf_2O_7$ at 800 nm [42–44].

III. CONCLUSIONS

We have prepared high-quality epitaxial $Yb_2Ti_2O_7$ films on YSZ single crystal substrates by pulsed laser deposition. XRD, RSM, AFM, and STEM characterization results show the high crystallinity and uniformity of $Yb_2Ti_2O_7$ films with atomic-scale epitaxy and sharp $Yb_2Ti_2O_7/YSZ$ interface. Interfacial strain and defects induced lattice distortion enhances magnetization, leading to the highest magnetization of $2.03\mu_B/Yb$ for the film fabricated at 10 Pa oxygen pressure. Moreover, the (001)-, (110)-, and (111)- epitaxial $Yb_2Ti_2O_7$ films exhibit a strong magnetic anisotropy, which mainly arises from the anisotropic exchange interactions and single ion anisotropy caused by local crystal field. In addition, optical transmission of approximately 95% was observed for the (110)-oriented $Yb_2Ti_2O_7$ films. These results lead to a comprehensive understanding of the magnetic anisotropy and structure-property relationships of transparent $Yb_2Ti_2O_7$ pyrochlore films.

[1] R. M. D'Ortenzio, H. A. Dabkowska, S. R. Dunsiger, B. D. Gaulin, M. J. P. Gingras, T. Goko, J. B. Kycia, L. Liu, T. Medina, T. J. Munsie, D. Pomaranski, K. A. Ross, Y. J. Uemura, T. J. Williams, and G. M. Luke, Phys. Rev. B **88**, 134428 (2013).

[2] A. Scheie, J. Kindervater, S. Säubert, C. Duvinage, C. Pfleiderer, H. J. Changlani, S. Zhang, L. Harriger, K. Arpino, S. M. Koohpayeh, O. Tchernyshyov, and C. Broholm, Phys. Rev. Lett. **119**, 127201 (2017).

[3] G. C. Lau, B. D. Muegge, T. M. McQueen, E. L. Duncan, and R. J. Cava, J. Solid State Chem. **179**, 3126 (2006).

[4] D. J. P. Morris, D. A. Tennant, S. A. Grigera, B. Klemke, C. Castelnovo, R. Moessner, C. Czternasty, M. Meissner, K. C. Rule, J. U. Hoffmann, K. Kiefer, S. Gerischer, D. Slobinsky, and R. S. Perry, Science **326**, 411 (2009).

[5] T. Fennell, P. P. Deen, A. R. Wildes, K. Schmalzl, D. Prabhakaran, A. T. Boothroyd, R. J. Aldus, D. F. McMorrow, and S. T. Bramwell, Science **326**, 415 (2009).

[6] L. Balents, Nature (London) **464**, 199 (2010).

[7] K. Momma and F. Izumi, J. Appl. Crystallogr. **44**, 1272 (2011).

[8] R. C. Ewing, W. J. Weber, and F. Lian, J. Appl. Phys. **95**, 5949 (2004).

[9] K. E. Arpino, B. A. Trump, A. O. Scheie, T. M. McQueen, and S. M. Koohpayeh, Phys. Rev. B **95**, 094407 (2017).

[10] N. R. Hayre, K. A. Ross, R. Applegate, T. Lin, R. R. P. Singh, B. D. Gaulin, and M. J. P. Gingras, Phys. Rev. B **87**, 184423 (2013).

[11] B. A. Trump, S. M. Koohpayeh, K. J. T. Livi, J. J. Wen, K. E. Arpino, Q. M. Ramasse, R. Brydson, M. Feygenson, H. Takeda, M. Takigawa, K. Kimura, S. Nakatsuji, C. L. Broholm, and T. M. McQueen, Nat. Commun. **9**, 2619 (2018).

[12] Y. Yasui, M. Soda, S. Iikubo, M. Ito, M. Sato, N. Hamaguchi, T. Matsushita, N. Wada, T. Takeuchi, N. Aso, and K. Kakurai, J. Phys. Soc. Jpn. **72**, 3014 (2003).

[13] K. A. Ross, L. R. Yaraskavitch, M. Laver, J. S. Gardner, J. A. Quilliam, S. Meng, J. B. Kycia, D. K. Singh, Th. Proffen, H. A. Dabkowska, and B. D. Gaulin, Phys. Rev. B **84**, 174442 (2011).

[14] J. A. Hodges, P. Bonville, A. Forget, A. Yaouanc, P. Dalmas de Réotier, G. André, M. Rams, K. Królas, C. Ritter, P. C. M. Grubbens, C. T. Kaiser, P. J. C. King, and C. Baines, Phys. Rev. Lett. **88**, 077204 (2002).

[15] J. Gaudet, D. D. Maharaj, G. Sala, E. Kermarrec, K. A. Ross, H. A. Dabkowska, A. I. Kolesnikov, G. E. Granroth, and B. D. Gaulin, Phys. Rev. B **92**, 134420 (2015).

[16] D. F. Bowman, E. Cemal1, T. Lehner, A. R. Wildes, L. Mangin-Thro, G. J. Nilsen, M. J. Gutmann, D. J. Voneshen, D. Prabhakaran, A. T. Boothroyd, D. G. Porter, C. Castelnovo, K. Refson, and J. P. Goff, Nat. Commun. **10**, 637 (2019).

[17] Z. L. Dun, M. Lee, E. S. Choi, A. M. Hallas, C. R. Wiebe, J. S. Gardner, E. Arrighi, R. S. Freitas, A. M. Arevalo-Lopez, J. P. Attfield, H. D. Zhou, and J. G. Cheng, Phys. Rev. B **89**, 064401 (2014).

[18] H. Cao, A. Gukasov, I. Mirebeau, P. Bonville, C. Decorse, and G. Dhalenne, Phys. Rev. Lett. **103**, 056402 (2009).

[19] B. Z. Malkin, T. T. A. Lummen, P. H. M. van Loosdrecht, G. Dhalenne, and A. R. Zakirov, J. Phys.: Condens. Matter **22**, 276003 (2010).

[20] E. Lhotel, S. R. Giblin, M. R. Lees, G. Balakrishnan, L. J. Chang, and Y. Yasui, Phys. Rev. B **89**, 224419 (2014).

[21] X. R. Liu, F. D. Wen, E. Karapetrova, J. W. Kim, P. J. Ryan, J. W. Freeland, M. Terilli, T. C. Wu, M. Kareev, and J. Chakhalian, Appl. Phys. Lett. **117**, 041903 (2020).

[22] V. K. Dwivedia and S. Mukhopadhyay, Physica B **571**, 137 (2019).

[23] See Supplemental Material at http://link.aps.org/supplemental/10.1103/PhysRevB.108.094105 for details about the experimental section and XRD patterns of $Yb_2Ti_2O_7$ ceramic target and $Yb_2Ti_2O_7$ films fabricated at different temperatures, AFM images and out-of-plane *M-H* curves of $Yb_2Ti_2O_7$ film fabricated at different oxygen pressures, AFM image and RSM of (110)-epitaxial $Yb_2Ti_2O_7$ film fabricated at 10 Pa, and XRD patterns of $Yb_2Ti_2O_7$ films fabricated on (001)- and (110)-YSZ substrates at 2×10^{-4} Pa.

[24] M. Ghosh, D. Samal, and P. S. Anil Kumar, Phys. Rev. B **106**, 085139 (2022).

[25] A. J. Hauser, J. R. Soliz, M. Dixit, R. E. A. Williams, M. A. Susner, B. Peters, L. M. Mier, T. L. Gustafson, M. D. Sumption, H. L. Fraser, P. M. Woodward, and F. Y. Yang, Phys. Rev. B **85**, 161201(R) (2012).

[26] W. L. Lu, P. Yang, W. D. Song, G. M. Chow, and J. S. Chen, Phys. Rev. B **88**, 214115 (2013).

[27] D. Gorkov, B. P. Toperverg, and H. Zabel, Phys. Rev. B **101**, 224404 (2020).

[28] J. C. Rojas Sanchez, B. Nelson-Cheeseman, M. Granada, E. Arenholz, and L. B. Steren, Phys. Rev. B **85**, 094427 (2012).

[29] A. M. Miller, M. Lemon, M. A. Choffel, S. R. Rich, F. Harvel, and D. C. Johnson, Z. Naturforsch. **77**, 313 (2022).

[30] K. Y. Chan and B. S. Teo, J Mater. Sci. **40**, 5971 (2005).

[31] L. Guo, N. Campbell, Y. Choi, J. W. Kim, P. J. Ryan, H. Huyan, L. Li, T. Nan, J. H. Kang, C. Sundahl, X. Pan, M. S. Rzchowski, and C. B. Eom, Phys. Rev. B **101**, 104405 (2020).

[32] S. T. Bramwell, M. N. Field, M. J. Harris, and I. P. Parkin, J. Phys.: Condens. Matter **12**, 483 (2000).

[33] J. A. Hodges, P. Bonville, A. Forget, M. Rams, K. Krolas, and G. Dhalenne, J. Phys.: Condens. Matter **13**, 9301 (2001).

[34] Q. J. Li, L. M. Xu, C. Fan, F. B. Zhang, Y. Y. Lv, B. Ni, Z. Y. Zhao, and X. F. Sun, J. Cryst. Growth **377**, 96 (2013).

[35] F. J. Ye, H. Y. Dai, K. Peng, T. Li, J. Chen, Z. P. Chen, and N. N. Li, J. Adv. Ceram. **9**, 444 (2020).

[36] S. J. Li, H. L. Che, J. C. Wu, X. Zhao, and X. F. Sun, AIP Adv. **8**, 055705 (2018).

[37] S. J. Li, Z. Y. Zhao, C. Fan, B. Tong, F. B. Zhang, J. Shi, J. C. Wu, X. G. Liu, H. D. Zhou, X. Zhao, and X. F. Sun, Phys. Rev. B **92**, 094408 (2015).

[38] J. S. Smart, *Effective Field Theories of Magnetism* (Saunders, London, 1966; Mir, Moscow, 1968).

[39] M. A. Subramanian, G. Aravamudan, and G. V. Subba Rao, Prog. Solid State Chem. **15**, 55 (1983).

[40] A. A. Biswas and Y. M. Jana, J. Magn. Magn. Mater. **323**, 3202 (2011).

[41] H. Y. Xiao, L. M. Wang, X. T. Zu, J. Lian, and R. C. Ewing, J. Phys.: Condens. Matter **19**, 346203 (2007).

[42] Z. J. Wang, X. J. Wang, G. H. Zhou, J. J. Xie, and S. W. Wang, J. Eur. Ceram. Soc. **39**, 3229 (2019).

[43] H. L. Yi, X. Q. Zou, Y. Yang, G. H. Zhou, and S. W. Wang, J. Am. Ceram. Soc. **94**, 4120 (2011).

[44] Z. J. Wang, G. H. Zhou, F. Zhang, X. P. Qin, J. P. Ai, and S. W. Wang, J. Lumin. **169**, 612 (2016).